



1 **Simultaneous OI 630 nm imaging observations of thermospheric gravity waves and**
2 **associated revival of fossil depletions around midnight near the EIA crest**

3
4

5 **Authors:**

6 **1. Navin Parihar**

7 Indian Institute of Geomagnetism, Navi Mumbai, India

8 e-mail: navindeparihar@gmail.com

9

10 **2. Saranya Padincharapad**

11 (a) Equatorial Geophysical Research Laboratory, Indian Institute of Geomagnetism,
12 Tirunelveli, India

13 (b) Manonmaniam Sundaranar University, Tirunelveli, India

14 e-mail: anuja8494@gmail.com

15

16 **3. Anand Kumar Singh**

17 National Centre for Polar and Ocean Research, Goa, India

18 e-mail: singhaaks@gmail.com

19

20

21

22

23

24 **Corresponding Author:**

25 **Navin Parihar**, Indian Institute of Geomagnetism, Navi Mumbai, India

26 e-mail: navindeparihar@gmail.com

27

28

29

30 **Key Words:**

31 Airglow imaging; Midnight Irregularities/Depletions; Gravity wave seeding; Low-
32 latitude ionosphere.

33



34 **Abstract**

35 We report the F-region airglow imaging of fossil plasma depletions around midnight that
36 revived afresh under the persisting thermospheric gravity wave (GW) activity. An all-sky
37 imager recorded these events in OI 630 nm imaging over Ranchi (23.3° N, 85.3° E, mlat. ~19°
38 N), India, on 16 April 2012. Northward propagating and east-west aligned GWs (λ ~210 km,
39 v ~64 m/s, and τ ~0.91 h) were seen around midnight. Persisting for ~2 hours, this GW
40 activity revived two co-existing and eastward drifting fossil depletions, DP1 and DP2. GWs-
41 driven revival was prominently seen in depletion DP1, wherein its apex height grew from
42 ~600 km to >800 km, and the level of intensity depletion increased from ~17% to 50%.
43 Present study is novel in the sense that simultaneous observations of thermospheric GWs
44 activity and associated evolution of depletion in OI 630 nm airglow imaging, and that too
45 around local midnight, have not been reported earlier. Current understanding is that GW
46 phase fronts aligned parallel to the geomagnetic field lines and eastward propagating are
47 more effective in seeding Rayleigh-Taylor (RT) instability. Here, GW fronts were east-west
48 aligned (i.e. perpendicular to the geomagnetic field lines) and propagated northward, yet they
49 revived fossil depletions.

50

51



52 1. Introduction

53 Gravity waves (GWs) are well-known to influence the mesosphere-lower thermosphere-
54 ionosphere (MLTI) region. GWs significantly contribute to the momentum and energy budget
55 of the MLT region via the wave-dissipation processes (Fritts and Alexander, 2003; Holton,
56 1983). Apart from the dominant solar and geomagnetic inputs, GWs are the key element in
57 some of the electrodynamic processes in the ionosphere e.g. irregularities, atmosphere-
58 ionosphere (AI) coupling, traveling ionospheric disturbances, etc.. In the equatorial F-region,
59 GWs modulate the ionospheric plasma into wave-like ionization structures. Under favourable
60 conditions, these structures act as a seed to Generalized Rayleigh-Taylor (GRT) instability
61 that generates the irregularities (Fritts et al., 2009; Huba and Joyce, 2007, 2010; Huba and
62 Liu, 2020; Hysell et al., 1990; Kelley, 2009; Woodman, 2009). GWs are also important in the
63 AI coupling during deep convection activity, thunderstorms, lightning, cyclones, tornadoes,
64 transient luminous events (TLEs)/sprites initiation, tsunami, etc. (Azeem and Barlage, 2018;
65 Maurya et al., 2022; Huba et al., 2015). GWs can also generate medium-scale traveling
66 ionospheric disturbances (MSTIDs) (Fukushima et al., 2012; Heale et al., 2022, and
67 references cited therein). On the course of their propagation, GWs can also induce periodic
68 fluctuations in the ionospheric parameters e.g. the electron density or total electron content
69 (TEC), the F-region height, temperatures and winds, etc. (Ford et al., 2006, 2008; Klausner et
70 al., 2009; Parihar et al., 2018; Vadas and Azeem, 2021) or airglow emission (Huba et al.,
71 2015; Makela et al., 2011).

72

73 The crucial role of GWs in seeding the post-sunset equatorial spread-F (ESF) or plasma
74 bubbles (EPBs) is fairly well understood (Abdu et al., 2009; Fritts et al., 2009; Huba and
75 Joyce, 2007, 2010; Hysell et al., 1990; Kelley, 2009; Singh et al., 1997; Tsunoda, 2010;
76 Tulasi Ram et al., 2014; Woodman, 2009). However, their role in the seeding of the
77 midnight/post-midnight irregularities remains poorly understood, especially when the
78 important criteria for the triggering of the GRT instability are absent (e.g., the favorable
79 alignment of the solar terminator with the geomagnetic field lines and the pre-reversal
80 enhancement, PRE, of the zonal electric field). Lately, Huba and Liu (2020) reported the
81 global simulations of the ESF using the SAMI3/WACCM-X coupled model. SAMI3 is the
82 abbreviation for ‘*Sami3 is Another Model of Ionosphere*’ (Huba et al., 2008), and WACCM-
83 X stands for the ‘*Whole Atmosphere Community Climate Model with thermosphere and*
84 *ionosphere extension*’ (Liu et al., 2010). For the first time, Huba and Liu’s (2020) simulations
85 demonstrated that GWs are the dominant seed mechanism and can spontaneously generate



86 the ESF, and that the EPBs develop self-consistently in the postsunset ionosphere. Studies by
87 Nishioka et al. (2012) show that the GRT instability can occur near midnight under the
88 influence of enhanced GW activity and then can lead to the growth of irregularities. MSTIDs
89 are an important generation mechanism of post-midnight irregularities wherein the electric
90 field perturbations associated with them acts as the seed (Miller et al., 2009; Taori et al.,
91 2015). Otsuka (2018) have presented an elaborative review of these mechanisms. All-sky
92 airglow imaging (ASAI) along with the radar, ionosonde, and GPS measurements have
93 significantly contributed to our understanding of the crucial role of GWs in seeding the EPBs
94 (Mendillo and Baumgardner, 1982; Mendillo et al., 1997; Taori et al., 2010; Yadav et al.,
95 2017). *Spread-F Experiment (SpreadFEx)* carried out in Brazil during September-November
96 2005 is one such example (Fritts et al., 2009). In the Indian subcontinent, Sreeja et al. (2009)
97 reported the GWs in OI 630 nm dayglow intensity variations that acted as a seed to the ESF
98 irregularities.

99

100 GWs that give rise to the EPBs have usually been reported in the MLT region airglow
101 imaging (e.g. Fritts et al., 2009; Paulino et al., 2011; Takahashi et al., 2009; Taori et al.,
102 2013). Reports featuring them in the F-region airglow imaging are rare and limited to that of
103 Makela et al. (2011), Paulino et al. (2016, 2018), Sau et al. (2018), and Smith et al. (2015).
104 Makela et al. (2011) and Smith et al. (2015) reported the thermospheric imaging observations
105 of GWs associated with tsunami and earthquake, respectively. Paulino et al. (2016, 2018) and
106 Sau et al. (2018) presented their observations in OI 630 nm imaging from Brazil and India,
107 respectively. However, these authors did not report any occurrence of depletions during the
108 undergoing GW activity. We report, for the first time, simultaneous observations GWs and
109 depletions in the F-region airglow imaging.

110

111 On the course of temporary campaign-based ASAI observations of OI 630 nm emission
112 under *Climate And Weather of Sun-Earth System (CAWSES) India Phase II Programme*
113 at Ranchi (23.3° N, 85.3° E, mlat. ~19° N), GW activity and “fossil depletions” were seen
114 together on 16 April 2012 with the former reviving the latter. Fossil depletions are the
115 remnants of airglow depletion or EPBs that have ceased growing upward or poleward;
116 however, they continue to persist and move with ambient plasma drift. Under *Maui Middle*
117 *Atmosphere and Lower Thermosphere (Maui-MALT)* initiative, Makela et al. (2004) reported
118 their extensive observations in OI 630 nm imaging from Haleakala Volcano (20.7° N, 203.7°
119 E; mlat. 21.3° N), Hawaii during the solar maximum of 2002-2003. Chapagain et al. (2011)



120 presented their limited observations from Christmas Island (2.1° N, 157.4° W, mlat. 2.8° N)
121 during September 1995. In India, Sekar et al. (2007) presented their case study from Gadanki
122 (13.5° N, 79.2° E, mlat. 6.3° N). However, these investigations did not discuss any
123 resurgence of fossil depletions associated with the GW activity. Novelty of this study is that
124 the “fossil depletions” revived into “active depletions” after the emission layer witnessed the
125 GW activity.

126

127

128 2. Instrumentation and data

129 Under the *CAWSES India Phase II Programme*, an ASAI was installed for limited
130 nightglow observations at Ranchi (23.3° N, 85.3° E, mlat. ~19° N), located near the crest of
131 equatorial ionization anomaly (EIA) in India during April 2012. Parihar et al. (2017) and
132 Parihar (2019) have presented an elaborative account of this ASAI system, the filter
133 characteristics of OI 630 nm emission imaging, the image processing technique, and the
134 limitations associated with the intensity calibration. Such GWs-driven revival of “fossil
135 depletions” was recorded in airglow images during 1700-2000 UT on 16 April 2012. Here,
136 Indian Standard Time (IST) = Universal Time (UT) + 0530 and Local Time (LT) ≈ IST. As
137 such, 1700-2000 UT corresponds to ~1.5 h duration before and after the local midnight. On
138 this night, the geomagnetic conditions were quiet with $Kp < 2$, $Ap = 4$, and $-4 < Dst < 10$
139 nT . We looked into the total electron content (TEC) measurements from an IGS station
140 Hyderabad (17.3° N, 78.6° E, mlat. ~12.0° N, located nearby and south of Ranchi) to support
141 the ASAI observations of GWs (Source: <https://t-ict4d.ictp.it/nequick2/gnss-tec-calibration>,
142 Ciruolo et al., 2007). Assuming that OI 630.0 nm emission peaks at 250 km and using known
143 astral positions, spatial displacement of depletions and GWs were determined from (i) the
144 intensity profiling along a desired direction in two successive images and (ii) the keogram
145 analysis. Pimenta et al. (2003) and Makela et al. (2006) have discussed these techniques,
146 respectively.

147

148 3. Observations

149 Figures 1 and 2 present airglow images that depict this event seen over Ranchi during 1742-
150 1942 UT on 16 April 2012. All-sky image’s timestamp information is in *hhmmss* format.
151 Fossil depletions of our interest that showed the GWs-driven revival are marked as **DP1** and
152 **DP2** in Figure 1 and 2. Here, **ROI1** is the region-of-interest wherein a few weakly



153 perceivable fronts of GWs and fossil depletions coexisted initially. Figure 3 shows the TEC
154 measurements depicting GW activity in and around Hyderabad during 1700-2000 UT on this
155 night.

156

157 **3.1 Signatures of GW activity in the F-region**

158 Faint signatures of GW activity were first seen near the southern edge of the field-of-view
159 (FOV) during ~1715-1724 UT. Starting ~1730 UT, their presence became more evident and
160 continued until 1906 UT or so. Some visible ones are marked as 'f1', 'f2', 'f3' and 'f4' in
161 Figure 1 and 2. North-south (NS) keograms [shown in Figure 3 (a) and (b)] showed
162 alternating bright and dark intensity striations over the north, and their slope indicates that
163 GWs propagated towards the north. Often GWs in OI 630 nm imaging are faint and unclear.
164 Under similar situations, time differenced images have proven ability to reflect them (Makela
165 et al., 2011). Presented in Figure 3 (c)-(d), time difference images show two GW fronts, 'f1'
166 and 'f2', separated by a dark trough during 1754-1806 UT. Being faint in nature, GWs
167 signatures in ASAI images were getting lost in the geographic unwarping process. We
168 estimated GWs propagation characteristics using the slope of striations in keograms and
169 cross-verified them with the intensity profiling technique. We found that these GWs
170 propagated from the south to north with the phase speed (v) of $\sim 64 \pm 2$ m/s and had the
171 horizontal wavelength (λ) and period (τ) of $\sim 210 \pm 6$ km and $\sim 0.91 \pm 0.06$ h, respectively.

172

173 Figure 3 (e) shows the scatter plots of the TEC along the trajectory of ionospheric pierce
174 points (IPPs) for different GPS satellites during 1700-2000 UT on this night. PRN numbers
175 of GPS satellites, along with the start time at 1700 UT, are indicated next to the
176 corresponding IPPs trajectory. TEC variations along the NS-aligned IPPs tracks (e.g. G27
177 and G28) clearly show the wavelike fluctuations in the 15-20° N latitude range. The temporal
178 evolution of the TEC for a few satellites is shown in Figure 3 (f). Of our interest is G28's
179 TEC measurement as its IPPs trajectory lay close to the imager's ROI1 during 1700-1800
180 UT. It showed a strong signature of GWs having $\tau \sim 0.95 \pm 0.03$ h, $\lambda \sim 229 \pm 12$ km, and v
181 $\sim 67 \pm 5$ m/s, and is in good agreement with the ASAI observations. The propagation
182 direction of GWs seen here is in good agreement with these previous reports. Studies on the
183 GW activity at the MLT heights over a farther low-latitude station Prayagraj (25.5° N,
184 formerly Allahabad) in India showed their propagation either northward or northeast around
185 midnight during April-May (Mukherjee et al., 2010). A comprehensive study of



186 thermospheric GWs in the ASAI observations over Tirunelveli (8.7° N) in India during 2013-
187 2015 indicated their propagation toward the north-northwest during the equinoxes (Sau et al.,
188 2018).

189

190 **3.2 GWs-driven revival of fossil depletions**

191 During 1730-1748 UT, faint signatures of depletion DP1 that revived were seen in the ROI1.
192 Depletion DP1 lacked any poleward growth during 1730-1806 UT. Using the equation given
193 in Kelley (2009) and by tracking the poleward tip of depletion, we estimated the apex height
194 of the associated geomagnetic flux tubes (A_H) and found it to be steady at ~600 km. Within it,
195 the level of intensity reduction with respect to that of the ambient region (i.e., $\Delta I/I_{\text{ambient region}}$)
196 was ~17 %. However, depletion DP1 drifted gradually to the east with a speed of 59-70 m/s.
197 Beginning 1812-1818 UT, this depletion started to intensify steadily, gain contrast against the
198 background and become noticeable. Southern end of depletion DP1 was fused with that of a
199 preceding depletion OD2. A few faint NS-aligned depletions were also present in the ROI1.
200 Along with depletion DP1, they intersected the EW-aligned fronts 'f1' and 'f2' of GWs, and
201 fragmented them into few isolated structures. Later on, these structures got attached to the
202 west wall of depletion DP1 and started moving in unison. Clear signs of two such fragments
203 (marked as S1 and S2 in Figure 1 and 2) can be seen at ~1830 UT and ~1806-1812 UT,
204 respectively. Starting 1824-1830 UT, we noted airglow enhancement to occur near its east
205 wall that then started to become distinct. As a result, an *inverted arrowhead*-shaped depletion
206 with an unusually wide southern fraction was evident during 1836-1854 UT. As two attached
207 structures S1 and S2 drifted along with depletion DP1, they tilted considerably to the east by
208 ~60-75° (see the ASAI images beginning 1830 UT in Figures 1 and 2). At ~1900 UT, the
209 structure S1 was almost aligned and merged with the west wall of depletion DP1, which led
210 to a fairly distinct west wall (seen as weak airglow enhancement). Airglow enhancement near
211 both the east and west wall (marked as A1 and A2, respectively, in Figure 2) continued, and a
212 linear NS-aligned depletion DP1 (having $A_H > 800$ km and $\Delta I/I_{\text{ambient region}} \sim 50$ %) was seen at
213 1906-1912 UT. Within the next 6-12 min, the apex of structure S2 merged with airglow
214 enhancement A2 near the west wall.

215

216 Next, some airglow enhancement occurred in the inner edge of the west wall of depletion
217 DP1 at 1924 UT (see the region-of-interest, ROI2 in Figure 2). We interpret this as a
218 consequence of some ambient plasma intrusion across its west wall. Otsuka et al. (2012) and



219 Shiokawa et al. (2015) earlier reported the disappearance of an EPB upon interaction with
220 MSTIDs and large-scale traveling ionospheric disturbances (LSTIDs), respectively. Authors
221 suggested that the electric field associated with MSTIDs/LSTIDs can move ambient plasma
222 into the bubble across the geomagnetic field line through $\mathbf{E} \times \mathbf{B}$ drift which will result in the
223 filling and subsequent disappearance of the depletion. We found that such intrusion, later, led
224 to the disappearance of its southern fraction and the formation of an isolated depletion at
225 1942 UT. Possibly these disappearances occurred due to the filling of the EIA plasma into
226 depletion across its western wall via the mechanism suggested by Otsuka et al. (2012).
227 Similarly, fossil depletion DP2 also revived; however, its evolution was much simpler than
228 that of depletion DP1.

229

230 **4 Discussions**

231 We present rare simultaneous observations of GWs activity and associated revival of fossil
232 depletions in the F-region airglow imaging around midnight over an off-equatorial station
233 Ranchi (located near the EIA crest) in India. Post-sunset ionospheric irregularities, in the
234 equatorial region, are generated by the GRT instability that sets off under the suitable
235 combination of (i) favourable alignment of solar terminator with geomagnetic field lines; (ii)
236 rapid height rise of the F-layer; (iii) absence of strong transequatorial wind and (iv) necessary
237 seed perturbation (Fejer and Kelley, 1980; Kelley, 2009; Makela and Otsuka, 2012;
238 Woodman, 2009). Stronger the height rise of the F-layer and an initial seed perturbation is,
239 the faster the growth rate of GRT instability, which ultimately leads to the rapid evolution of
240 the irregularities (Huba and Joyce, 2007; Huang et al., 1993; Hysell et al., 2014; Kelley et al.,
241 1981; Krall et al., 2013; Tsunoda, 2010; Zalesak and Ossakow, 1980). GWs are well known
242 to deform the bottom side plasma of the F-region into the wavelike ionization structures that
243 then act as a seed to GRT instability, which, in turn, generates irregularities. While their role
244 in the generation of the post-sunset irregularities is well known, our understanding is limited
245 in the context of midnight/post-midnight irregularities. Present study features midnight fossil
246 airglow depletions that revived due to undergoing GW activity and turned into an active
247 depletion.

248

249 Northward propagating GWs having $\lambda \sim 210$ km, $v \sim 64$ m/s, and $\tau \sim 0.91$ h were recorded in
250 630 nm nightglow images during 1715-1906 UT. Supporting airglow observations, TEC
251 measurements, too, showed the presence of similar GWs. Simultaneously, an eastward



252 drifting fossil depletion DP1 ($A_H \sim 600$ km and $\Delta I/I_{\text{ambient region}} \sim 17$ %) co-existed during
253 1730-1748 UT. Next, depletion DP1 and other co-existing depletions intercepted EW-aligned
254 GW fronts and fragmented them during 1806-1824 UT. Subsequently, two such fragments
255 viz. S1 and S2 that lay close to depletion DP1 got attached to its west wall, started drifting
256 eastward in unison, tilted significantly to the east, and almost got aligned with the west wall.
257 Next, depletion DP1 gradually intensified, surged polewards, and became a well-developed
258 linear depletion ($A_H > 800$ km and $\Delta I/I_{\text{ambient region}} \sim 50$ %) during 1906-1912 UT. Meanwhile,
259 airglow enhancement continued to develop near both its walls and an uneven broadening was
260 seen in its southern half. Next, some ambient plasma diffusion occurred near this uneven
261 region leading to airglow enhancement in the inner edge of its west wall at 1924 UT. Such
262 intrusion continued, its southern fraction gradually disappeared, and an isolated depletion was
263 formed at 1942 UT. Present observations clearly indicate that “fossil depletion” DP1 revived
264 and became an “active depletion” under the influence of co-existing GWs activity. Another
265 succeeding depletion, DP2, too, showed a similar revival.

266

267 An important consideration in the GWs seeding of the GRT instability is the alignment of
268 their wavefronts with the geomagnetic field lines. The current understanding is that the
269 strength of the polarization electric field generated by the GWs greatly depends on the angle
270 between them, and the maximum polarization occurs when their wavefront is aligned with the
271 geomagnetic field (Huba et al., 2015; Hysell et al., 2014; Krall et al., 2013; Tulasi Ram et al.,
272 2014; Tsunoda, 2010). Numerical simulations by Hysell et al. (2014) suggest that the GWs-
273 induced modulations were the most severe when their fronts were aligned with the magnetic
274 meridian. Using Communications/Navigation Outrage Forecasting System (C/NOFS) mission
275 TEC measurements, Tulasi Ram et al. (2014) studied the characteristics of large-scale wave
276 structure (LSWS) at the base of the F-region and their association with the EPBs occurrences
277 in Southeast Asia and Africa. Authors found that the EPBs frequently occurred when the
278 amplitudes of LSWS were adequately increased, and their phase fronts were geomagnetic
279 field-aligned.

280

281 In the present study, the GWs fronts were east-west aligned (i.e., transverse to the
282 geomagnetic field lines) and propagated northward. Yet, fossil depletions DP1 and DP2
283 revived and is intriguing. Meridional wind perturbations associated with GWs are known to
284 be ineffective in the initiation and development of depletions. Present observations are in



285 contrast with this notion and point towards another excitation mechanism rather than GRT
286 instability, which we conjecture, is the spatial resonance mechanism for these reasons. Good
287 matching was seen between the GWs phase speed ($v \sim 64\text{--}67$ m/s) and the eastward drift of
288 depletion DP1 ($v \sim 59\text{--}70$ m/s). Horizontal Wind Model 2007 estimates also indicated the
289 zonal thermospheric wind speed of 51-61 m/s (Drob et al., 2008). We estimated the speed at
290 which the apex of DP1 progressed poleward and found it to be in the range of 46-56 m/s.
291 Spatial resonance theory of GWs seeding of irregularities states that the effects of GWs
292 perturbations are the strongest when its phase speed and the plasma drift velocity are nearly
293 equal (Kelley et al., 1981). Under such conditions, the ionospheric plasma exerts the GW-
294 associated forcing for a longer duration; thereby, accelerating the formation of ionization
295 structures. As such, we conjecture that this GWs-driven revival of fossil depletions occurred
296 via the spatial resonance mechanism. Numerical simulations by Huang and Kelley (1996)
297 suggest that this mechanism can accelerate the formation of depletions. Possibly continuously
298 undergoing GWs activity for 2 hours in the F-region sufficiently intensified the magnitude of
299 associated ionization modulations, which in turn triggered and sustained the revival of fossil
300 depletions via the spatially resonant mechanism.

301

302 Meridional wind can influence the growth rate of GRT instability by altering the field-line
303 integrated Pederson conductivity. Maruyama (1988) and Abdu et al. (2006) found that strong
304 meridional winds could reduce the growth rate of RTI and suppress irregularities. Huba and
305 Krall (2013) have reported both stabilizing and destabilizing effects of the meridional winds
306 on RT instability. Devasia et al. (2002) found that a suitable combination of the meridional
307 wind and F-region base height favours ESF development. In the present study, the meridional
308 wind measurements using a Fabry-Perot interferometer, etc. were not available; hence, their
309 possible role in the evolution of these fossil depletions could not be investigated.

310

311 **5 Summary**

312 We present, here, airglow imaging observations of fossil plasma depletions that revived
313 afresh under the action of prolonged GW activity and became active depletions. Such
314 simultaneous imaging of thermospheric GWs and depletions was recorded in the ASAI of OI
315 630 nm emission over Ranchi (mlat. $\sim 19^\circ$ N), India, on 16 April 2012. Salient features of the
316 present study are as under:



- 317 1. First, airglow images showed EW-aligned and SN-propagating GWs ($\lambda \sim 210$ km, v
318 ~ 64 m/s, and $\tau \sim 0.91$ h) over Ranchi during 1715-1906 UT. Similar GWs were, also,
319 seen in TEC measurements over a lower latitude station Hyderabad.
- 320 2. A co-existing and prominent fossil depletion DP1 revived under this GW activity
321 wherein its apex raised from 600 km to >800 km, and the level of intensity depletion
322 increased from 17 % to 50 %. Another fossil depletion DP2, too, revived.
323 Interestingly, GWs phase fronts were transverse to the geomagnetic field lines, yet
324 two fossil depletions revived under their influence and became active depletions.
- 325 3. As GWs phase speed ($v \sim 64$ -67 m/s) nearly matched the eastward drift of depletion
326 DP1 ($v \sim 59$ -70 m/s), we conjecture that the GWs-driven revival of these fossil
327 depletions possibly occurred via the spatial resonance mechanism.
- 328 4. An uneven region of increased thickness existed on the southern half of the revived
329 depletion DP1, wherein some airglow enhancement was seen later in the inner edge of
330 its west wall. Possibly the gradual disappearance of its southern fraction occurred
331 because of the intrusion of ambient plasma across the west wall.

332

333 Contrary to the current understanding, this study shows that the GWs fronts aligned
334 perpendicular to the geomagnetic field lines can effectively grow irregularities. Present
335 observations of the GWs-driven revival of fossil airglow depletions further contribute to our
336 understanding of their generation mechanism around midnight.

337

338

339 **Data Availability.** Airglow data used in the present study are available through the
340 institutional data repository (<http://www.iigm.res.in/>) or
341 <https://doi.org/10.5281/zenodo.8143215>. Calibrated TEC data is available from [https://t-](https://t-ict4d.ictp.it/nequick2/gnss-tec-calibration)
342 [ict4d.ictp.it/nequick2/gnss-tec-calibration](https://t-ict4d.ictp.it/nequick2/gnss-tec-calibration).

343

344

345 **Author contributions.** NP conceptualized the research problem and prepared the first draft.
346 All authors contributed to the interpretation of results, discussion, and subsequent drafting of
347 the manuscript.

348

349



350 **Acknowledgements:** Funds for Airglow Research at *Indian Institute of Geomagnetism* are
351 being provided by *Department of Science and Technology (DST), Govt. of India, New*
352 *Delhi*. GNSS TEC Calibrated data were downloaded from [https://t-](https://t-ict4d.ictp.it/nequick2/gnss-tec-calibration)
353 [ict4d.ictp.it/nequick2/gnss-tec-calibration](https://t-ict4d.ictp.it/nequick2/gnss-tec-calibration) and *Telecommunications/ICT for Development*
354 *(T/ICT4D) Laboratory of the Abdus Salam International Centre for Theoretical Physics,*
355 *Trieste, Italy* is gratefully acknowledged. *SP* is grateful to *Director, Indian Institute of*
356 *Geomagnetism, Navi Mumbai* for the award of Research Scholarship.

357

358

359 **References:**

360 Abdu, M., Iyer, K. N., de Medeiros, R., Batista, I. S. and Sobral, J. H.: Thermospheric
361 meridional wind control of equatorial spread F and evening prereversal electric field,
362 *Geophys. Res. Lett.* 33 (7). <http://dx.doi.org/10.1029/2005GL024835>, 2006.

363

364 Abdu, M. A., Kherani, E. A., Batista, I. S., de Paula, E. R., Fritts, D. C., and Sobral, J. H.:
365 Gravity wave initiation of equatorial spread F/plasma bubble irregularities based on
366 observational data from the SpreadFEx campaign, *Ann. Geophys.*, 27, 2607-2622.
367 <https://doi.org/10.5194/angeo-27-2607-2009>, 2009.

368

369 Azeem, I., and Barlage, M.: Atmosphere-ionosphere coupling from convectively generated
370 gravity waves. *Adv. Space Res.*, 61(7), 1931-1941. <https://doi.org/10.1016/j.asr.2017.09.029>,
371 2018.

372

373 Ciruolo, L., Azpilicueta, F., Brunini, C., Meza, A. and Radicella, S. M.: Calibration errors on
374 experimental slant total electron content (TEC) determined with GPS. *J. Geod.*, 81, 111–120,
375 <https://doi.org/10.1007/s00190-006-0093-1>, 2007.

376

377 Chapagain, N. P., Taylor, M. J., and Eccles, J. V.: Airglow observations and modeling of F
378 region depletion zonal velocities over Christmas Island, *J. Geophys. Res.*, 116, A02301,
379 <https://doi.org/10.1029/2010JA015958>, 2011.

380

381 Devasia, C., Jyoti, N., Subbarao, K., Viswanathan, K., Tiwari, D. and Sridharan, R.: On the
382 plausible linkage of thermospheric meridional winds with the equatorial spread F, *J. Atmos.*
383 *Sol.-Terrest. Phys.* 64 (1), 1–12, [http://dx.doi.org/10.1016/S1364-6826\(01\)00089-X](http://dx.doi.org/10.1016/S1364-6826(01)00089-X), 2002.



384

385 Drob, D. P., Emmert, J. T., Crowley, G., Picone, J. M., Shepherd, G. G., Skinner, W., et al.:
386 An empirical model of the Earth's horizontal wind fields: HWM07. *J. Geophys. Res.*, 113,
387 A12304, <https://doi.org/10.1029/2008JA013668>, 2008.

388

389 Fejer, B. G., and Kelley, M. C.: Ionospheric irregularities. *Rev. Geophys.*, 18(2), 401-454,
390 <https://doi.org/10.1029/RG018i002p00401>, 1980.

391

392 Ford, E. A. K., Aruliah, A. L., Griffin, E. M., and McWhirter, I.: Thermospheric gravity
393 waves in Fabry-Perot Interferometer measurements of the 630.0nm OI line, *Ann. Geophys.*,
394 24, 555–566, <https://doi.org/10.5194/angeo-24-555-2006>, 2006.

395

396 Ford, E. A. K., Aruliah, A. L., Griffin, E. M., and McWhirter, I.: Statistical analysis of
397 thermospheric gravity waves from Fabry-Perot Interferometer measurements of atomic
398 oxygen, *Ann. Geophys.*, 26, 29–45, <https://doi.org/10.5194/angeo-26-29-2008>, 2008.

399

400 Fritts, D. C., and Alexander, M. J.: Gravity wave dynamics and effects in the middle
401 atmosphere, *Rev. Geophys.*, 41, 1003, <https://doi.org/10.1029/2001RG000106>, 1, 2003.

402

403 Fritts, D. C., Abdu, M. A., Batista, B. R., Batista, I. S., Batista, P. P., Buriti, R., Clemesha, B.
404 R., Dautermann, T., de Paula, E. R., Fechine, B. J., Fejer, B. G., Gobbi, D., Haase, J.,
405 Kamalabadi, F., Kherani, E. A., Laughman, B., Lima, P. P., Liu, H.-L., Medeiros, A., Pautet,
406 P.-D., Rigglin, D. M., Rodrigues, F. S., São Sabbas, F., Sobral, J. H. A., Stamus, P.,
407 Takahashi, H., Taylor, M. J., Vadas, S. L., Vargas, F., and Wrasse, C. M.: Overview and
408 summary of the Spread F Experiment (SpreadFEx), *Ann. Geophys.*, 27, 2141–2155,
409 <https://doi.org/10.5194/angeo-27-2141-2009>, 2009.

410

411 Fukushima, D., Shiokawa, K., Otsuka, Y., and Ogawa, T.: Observation of equatorial
412 nighttime medium-scale traveling ionospheric disturbances in 630-nm airglow images over 7
413 years. *J. Geophys. Res.*, 117, A10324. <https://doi.org/10.1029/2012JA017758>, 2012.

414

415 Heale, C. J., Inchin, P. A., and Snively, J. B.: Primary versus secondary gravity wave
416 responses at F-region heights generated by a convective source, *J. Geophys. Res. Space*
417 *Physics*, 127, e2021JA029947, <https://doi.org/10.1029/2021JA029947>, 2022.



418

419 Huang, C.-S., Kelley, M. C., and Hysell, D. L.: Nonlinear Rayleigh-Taylor instabilities,
420 atmospheric gravity waves and equatorial spread F, *J. Geophys. Res.*, 98(A9), 15631-15642,
421 <https://doi.org/10.1029/93JA00762>, 1993.

422

423 Huang, C.-S., and Kelley, M. C.: Nonlinear evolution of equatorial spread F: 1. On the role of
424 plasma instabilities and spatial resonance associated with gravity wave seeding, *J. Geophys.*
425 *Res.*, 101(A1), 283-292, <https://doi.org/10.1029/95JA02211>, 1996.

426

427 Huba, J. D., and Joyce, G.: Equatorial spread F modeling: Multiple bifurcated structures,
428 secondary instabilities, large density ‘bite-outs’ and supersonic flows. *Geophys. Res. Lett.*,
429 34, L07105. <https://doi.org/10.1029/2006GL028519>, 2007.

430

431 Huba, J. D., Joyce, G., and Krall, J.: Three-dimensional equatorial spread F modeling,
432 *Geophys. Res. Lett.*, 35, L10102. <https://doi.org/10.1029/2008GL033509>, 2008.

433

434 Huba, J. D., and Joyce, G.: Global modeling of equatorial plasma bubbles, *Geophys. Res.*
435 *Lett.*, 37, L17104, <https://doi.org/10.1029/2010GL044281>, 2010.

436

437 Huba, J. D., and Krall, J.: Impact of meridional winds on equatorial spread F: Revisited,
438 *Geophys. Res. Lett.*, 40, 1268– 1272, doi:10.1002/grl.50292, 2013.

439

440 Huba, J. D., Drob, D. P., Wu, T.-W., and Makela, J. J.: Modeling the ionospheric impact of
441 tsunami-driven gravity waves with SAMI3: Conjugate effects. *Geophys. Res. Lett.*, 42,
442 5719–5726. <https://doi.org/10.1002/2015GL064871>, 2015.

443

444 Huba, J. D., and Liu, H.-L.: Global modeling of equatorial spread F with SAMI3/WACCM-
445 X. *Geophys. Res. Lett.*, 47, e2020GL088258. <https://doi.org/10.1029/2020GL088258>, 2020.

446

447 Hysell, D. L., Kelley, M. C., Swartz, W. E., and Woodman, R. F.: Seeding and layering of
448 equatorial spread F by gravity waves. *J. Geophys. Res.*, 95(A10), 17,253-17,260.
449 <https://doi.org/10.1029/JA095iA10p17253>, 1990.

450



- 451 Hysell, D. L., Jafari, R., Fritts, D. C., and Laughman, B.: Gravity wave effects on postsunset
452 equatorial F region stability, *J. Geophys. Res. Space Physics*, 119, 5847– 5860,
453 doi:10.1002/2014JA019990, 2014.
454
- 455 Kelley, M. C., Larsen, M. F., LaHoz, C., and McClure, J. P.: Gravity wave initiation of
456 equatorial spread F: A case study, *J. Geophys. Res.*, 86 (A11), 9087-9100,
457 <https://doi.org/10.1029/JA086iA11p09087>, 1981.
458
- 459 Kelley, M. C.: *The Earth's ionosphere: Plasma physics and electrodynamics* (2nd ed.).
460 Burlington, MA: Elsevier, 2009.
461
- 462 Klausner, V., Fagundes, P. R., Sahai, Y., Wrasse, C. M., Pillat, V. G., and Becker-Guedes, F.:
463 Observations of GW/TID oscillations in the F2 layer at low latitude during high and low solar
464 activity, geomagnetic quiet and disturbed periods, *J. Geophys. Res.*, 114, A02313,
465 <https://doi.org/10.1029/2008JA013448>, 2009.
466
- 467 Krall, J., Huba, J. D., and Fritts, D. C.: On the seeding of equatorial spread F by gravity
468 waves, *Geophys. Res. Lett.*, 40, 661-664, <https://doi.org/10.1002/grl.50144>, 2013.
469
- 470 Makela, J. J., Ledvina, B. M., Kelley, M. C. and. Kintner, P. M: Analysis of the seasonal
471 variations of equatorial plasma bubble occurrence observed from Haleakala, Hawaii, *Ann.*
472 *Geophys.*, 22, 3109-3121, <https://doi.org/10.5194/angeo-22-3109-2004>, 2004.
473
- 474 Makela, J. J., Kelley, M. C., and Nicolls, M. J.: Optical observations of the development of
475 secondary instabilities on the eastern wall of an equatorial plasma bubble. *J. Geophys. Res.*,
476 111, A09311, <https://doi.org/10.1029/2006JA011646>, 2006.
477
- 478 Makela, J. J., Lognonne, P., Hebert, H., Gehrels, T., Rolland, L., Allgeyer, S., et al.: Imaging
479 and modeling the ionospheric airglow response over Hawaii to the tsunami generated by the
480 Tohoku earthquake of 11 March 2011. *Geophys. Res. Lett.*, 38, L00G02.
481 <https://doi.org/10.1029/2011GL047860>, 2011.
482



- 483 Makela, J. J., and Otsuka, Y.: Overview of nighttime ionospheric instabilities at low- and
484 mid-latitudes: Coupling aspects resulting in structuring at the mesoscale. *Space Sci. Rev.*,
485 168(1-4), 419-440. <https://doi.org/10.1007/s11214-011-9816-6>, 2012.
486
- 487 Maruyama, T.: A diagnostic model for equatorial spread F: 1. Model description and
488 application to electric field and neutral wind effects, *J. Geophys. Res.*, 93 (A12), 14611–
489 14622. <http://dx.doi.org/10.1029/JA093iA12p14611>, 1988.
490
- 491 Maurya, A. K., Parihar, N., Dube, A., Singh, R., Kumar, S., Chanrion, O., Tomicic, M., and
492 Neubert, T.: Rare observations of sprites and gravity waves supporting D, E, F-regions
493 ionospheric coupling, *Sci. Rep.*, 12, 581. <https://doi.org/10.1038/s41598-021-03808-5>, 2022.
494
- 495 Mendillo, M., and Baumgardner, J.: Airglow characteristics of equatorial plasma depletions.
496 *J. Geophys. Res.*, 87, 7641-7652, <https://doi.org/10.1029/JA087iA09p07641>, 1982.
497
- 498 Mendillo, M., Baumgardner, J., Colerico, M., and Nottingham, D.: Imaging science
499 contributions to equatorial aeronomy: initial results from the MISETA program, *J. Atmos.*
500 *Terr. Phys.*, 59, 1587-1599, [https://doi.org/10.1016/S1364-6826\(96\)00158-7](https://doi.org/10.1016/S1364-6826(96)00158-7), 1997.
501
- 502 Miller, E. S., Makela, J. J., and Kelley, M. C.: Seeding of equatorial plasma depletions by
503 polarization electric fields from middle latitudes: Experimental evidence, *Geophys. Res.*
504 *Let.*, 36, L18105, <https://doi.org/10.1029/2009GL039695>, 2009.
505
- 506 Mukherjee, G. K., Pragati Shikha, R., Parihar, N., Ghodpage, R. and Patil, P. T.: Studies of
507 the wind filtering effect of gravity waves observed at Allahabad (25.45° N, 81.85° E). *Earth*
508 *Planets Space* 62, 309-318, <https://doi.org/10.5047/eps.2009.11.008>, 2010.
509
- 510 Nishioka, M., Otsuka, Y., Shiokawa, K., Tsugawa, T., Effendy, , Supnithi, P., Nagatsuma, T.,
511 and Murata, K. T.: On post-midnight field-aligned irregularities observed with a 30.8-MHz
512 radar at a low latitude: Comparison with F-layer altitude near the geomagnetic equator, *J.*
513 *Geophys. Res.*, 117, A08337, <https://doi.org/10.1029/2012JA017692>, 2012.
514



- 515 Otsuka, Y., Shiokawa, K. and Ogawa, T.: Disappearance of equatorial plasma bubble after
516 interaction with mid-latitude medium-scale traveling ionospheric disturbance, *Geophysical*
517 *Research Letters*, 39, L14105, <https://doi.org/10.1029/2012GL052286>, 2012.
- 518
- 519 Otsuka, Y.: Review of the generation mechanisms of post-midnight irregularities in the
520 equatorial and low-latitude ionosphere. *Prog. Earth Planet. Sci.* 5, 57.
521 <https://doi.org/10.1186/s40645-018-0212-7>, 2018.
- 522
- 523 Parihar, N., Singh, D., and Gurubaran, S.: A comparison of ground-based hydroxyl airglow
524 temperatures with SABER/TIMED measurements over 23° N, India, *Ann. Geophys.*, 35,
525 353–363, <https://doi.org/10.5194/angeo-35-353-2017>, 2017.
- 526
- 527 Parihar, N., Radicella, S. M., Nava, B., Migoya-Orue, Y. O., Tiwari, P., and Singh, R.: An
528 investigation of the ionospheric F region near the EIA crest in India using OI 777.4 and 630.0
529 nm nightglow observations. *Ann. Geophys.*, 36(3), 809-823. [https://doi.org/10.5194/angeo-](https://doi.org/10.5194/angeo-36-809-2018)
530 [36-809-2018](https://doi.org/10.5194/angeo-36-809-2018), 2018.
- 531
- 532 Parihar, N.: Rare occurrence of off-equatorial edge initiating and equatorward surging plasma
533 depletions observed in OI 630-nm imaging. *J. Geophys. Res. Space Physics*, 124, 2887-2896.
534 <https://doi.org/10.1029/2018JA026155>, 2019.
- 535
- 536 Paulino, I., Takahashi, H., Medeiros, A. F., Wrasse, C. M., Buriti, R. A., Sobral, J. H. A., and
537 Gobbi, D.: Mesospheric gravity waves and ionospheric plasma bubbles observed during the
538 COPEX campaign. *J. Atmos. Sol.-Terr. Phys.*, 73(11-12), 1575-1580.
539 <https://doi.org/10.1016/j.jastp.2010.12.004>, 2011.
- 540
- 541 Paulino, I., Medeiros, A. F., Vadas, S. L., Wrasse, C. M., Takahashi, H., Buriti, R. A., Leite,
542 D., Filgueira, S., Bageston, J. V., Sobral, J. H. A., and Gobbi, D.: Periodic waves in the lower
543 thermosphere observed by OI630 nm airglow images, *Ann. Geophys.*, 34, 293-301,
544 <https://doi.org/10.5194/angeo-34-293-2016>, 2016.
- 545
- 546 Paulino, I., Moraes, J. F., Maranhão, G. L., Wrasse, C. M., Buriti, R. A., Medeiros, A. F.,
547 Paulino, A. R., Takahashi, H., Makela, J. J., Meriwether, J. W., and Campos, J. A. V.:
548 Intrinsic parameters of periodic waves observed in the OI6300 airglow layer over the



- 549 Brazilian equatorial region, *Ann. Geophys.*, 36, 265–273, <https://doi.org/10.5194/angeo-36->
550 265-2018, 2018.
- 551
- 552 Pimenta, A. A., Fagundes, P. R., Sahai, Y., Bittencourt, J. A., and Abalde, J. R.: Equatorial F-
553 region plasma depletion drifts: latitudinal and seasonal variations. *Ann. Geophys.*, 21, 2315-
554 2322, <https://doi.org/10.5194/angeo-21-2315-2003>, 2003.
- 555
- 556 Sau, S., Narayanan, V. L., Gurubaran, S., and Emperumal, K.: Study of wave signatures
557 observed in thermospheric airglow imaging over the dip equatorial region. *Adv. Space Res.*,
558 62(7), 1762–1774, <https://doi.org/10.1016/j.asr.2018.06.039>, 2018.
- 559
- 560 Sekar, R., Chakrabarty, D., Sarkhel, S., Patra, A. K., Devasia, C. V., and Kelley, M. C.:
561 Identification of active fossil bubbles based on coordinated VHF radar and airglow
562 measurements, *Ann. Geophys.*, 25, 2099-2102, <https://doi.org/10.5194/angeo-25-2099-2007>,
563 2007.
- 564
- 565 Shiokawa, K., Otsuka, Y., Lynn, K. J., Wilkinson, P., and Tsugawa, T.: Airglow-imaging
566 observation of plasma bubble disappearance at geomagnetically conjugate points. *Earth*
567 *Planets and Space*, 67(1), 43, <https://doi.org/10.1186/s40623-015-0202-6>, 2015.
- 568
- 569 Singh, S., Johnson, F. S., and Power, R. A.: Gravity wave seeding of equatorial plasma
570 bubbles. *J. Geophys. Res.*, 102(A4), 7399– 7410, <https://doi.org/10.1029/96JA03998>, 1997.
- 571
- 572 Smith, S. M., Martinis, C. R., Baumgardner, J., and Mendillo, M.: All-sky imaging of
573 transglobal thermospheric gravity waves generated by the March 2011 Tohoku Earthquake, *J.*
574 *Geophys. Res. Space Physics*, 120, 10,992-10,999, <https://doi.org/10.1002/2015JA021638>,
575 2015.
- 576
- 577 Sreeja, V., Vineeth, C., Pant, T. K., Ravindran, S. and Sridharan, R.: Role of gravity wavelike
578 seed perturbations on the triggering of ESF-First results from unique dayglow observations,
579 *Ann. Geophys.*, 27, 313-318, <https://doi.org/10.5194/angeo-27-313-2009>, 2009.
- 580
- 581 Takahashi, H., Taylor, M. J., Pautet, P.-D., Medeiros, A. F., Gobbi, D., Wrasse, C. M.,
582 Fechine, J., Abdu, M. A., Batista, I. S., Paula, E., Sobral, J. H. A., Arruda, D., Vadas, S. L.,



- 583 Sabbas, F. S., and Fritts, D. C.: Simultaneous observation of ionospheric plasma bubbles and
584 mesospheric gravity waves during the SpreadFEx Campaign, *Ann. Geophys.*, 27, 1477-1487,
585 <https://doi.org/10.5194/angeo-27-1477-2009>, 2009.
586
- 587 Taori, A., Makela, J. J., and Taylor, M. J.: Mesospheric wave signatures and equatorial
588 plasma bubbles: A case study, *J. Geophys. Res.*, 115, A6, A06302,
589 <https://doi.org/10.1029/2009JA015088>, 2010.
590
- 591 Taori, A., Jayaraman, A., and Kamalakar, V.: Imaging of mesosphere-thermosphere airglow
592 emissions over Gadanki (13.5° N, 79.2° E): First results. *J. Atmos. Sol.-Terr. Phys.*, 93, 21-
593 28. <https://doi.org/10.1016/j.jastp.2012.11.007>, 2013.
594
- 595 Taori, A., Parihar, N., Ghodpage, R., Dashora, N., Sripathi, S., Kherani, E. A., and Patil, P. T.
596 (2015). Probing the possible trigger mechanisms of an equatorial plasma bubble event based
597 on multistation optical data. *J. Geophys. Res. Space Physics*, 120, 8835-8847.
598 <https://doi.org/10.1002/2015JA021541>.
599
- 600 Tsunoda, R. T.: On seeding equatorial spread F: Circular gravity waves, *Geophys. Res. Lett.*,
601 37, L10104, <https://doi.org/10.1029/2010GL043422>, 2010.
602
- 603 Tulasi Ram, S., Yamamoto, M., Tsunoda, R. T., Chau, H. D., Hoang, T. L., Dantie, B.,
604 Wassae, M., Yatini, C. Y., Manik, T., and Tsugawa, T.: Characteristics of large-scale wave
605 structure observed from African and Southeast Asian longitudinal sectors, *J. Geophys. Res.*
606 *Space Physics*, 119, 2288-2297, <https://doi.org/10.1002/2013JA019712>, 2014.
607
- 608 Vadas, S. L., and Azeem, I.: Concentric secondary gravity waves in the thermosphere and
609 ionosphere over the continental United States on 25-26 march 2015 from deep convection. *J.*
610 *Geophys. Res. Space Physics*, 126, e2020JA028275. <https://doi.org/10.1029/2020JA028275>,
611 2021.
612
- 613 Woodman, R. F.: Spread F: An old equatorial aeronomy problem finally resolved? *Ann.*
614 *Geophys.*, 27(5), 1915-1934. <https://doi.org/10.5194/angeo-27-1915-2009>, 2009.
615



616 Yadav, S., Sridharan, R., Sunda, S. and Pant, T. K.: Further refinements to the spatiotemporal
617 forecast model for L-band scintillation based on comparison with C/NOFS observations, *J.*
618 *Geophys. Res. Space Physics*, 122, 5643-5652, <https://doi.org/10.1002/2017JA023869>, 2017.
619
620 Zalesak, S., and Ossakow, S.: Nonlinear equatorial spread F: Spatially large bubbles resulting
621 from large horizontal scale initial perturbations. *J. Geophys. Res.*, 85(A5), 2131-2142.
622 <https://doi.org/10.1029/JA085iA05p02131>, 1980.
623



624 **Figure Captions**

625 **Figure 1.** ASAI images during 1742-1830 UT over Ranchi (23.3° N, 85.3° E, mlat. ~19° N)
626 on 16 April 2012. DP1 is the first fossil plasma depletion that showed GWs driven revival.
627 Depletions OD1 and OD2 preceded depletion DP1. ROI1 is the region-of-interest wherein the
628 south-north propagating GW activity and faint signatures of eastward drifting depletion DP1
629 were seen initially. Some noticeable GWs fronts are 'f1', 'f2' and 'f3' (in succession). 'S1'
630 and 'S2' are the fractions of fronts 'f1' and 'f2', respectively, that subsequently got linked to
631 the west wall of depletion DP1.

632

633 **Figure 2.** Same as Figure 1 but for 1836-1942 UT. DP2 is the second fossil depletion that
634 showed GWs driven revival. Some noticeable GWs fronts are 'f3' and 'f4'. A1 and A2 are
635 two arc-shaped regions of airglow enhancement near the east and west wall of depletion DP1.
636 ROI2 is the region-of-interest wherein ambient plasma diffusion occurred across the west
637 wall of depletions DP1.

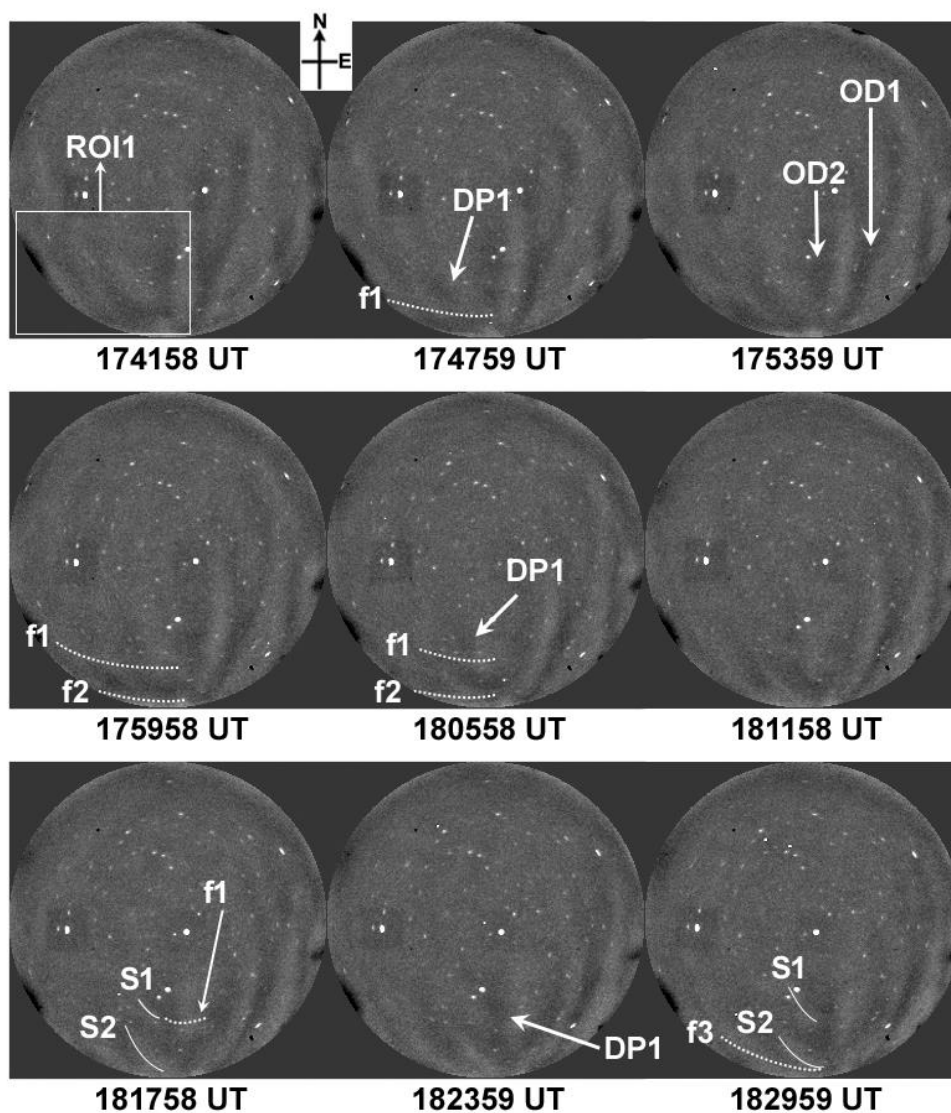
638

639 **Figure 3.** (a)-(b) North-south (NS) keogram along 84.4° E and 85.3° E longitude generated
640 from OI 630 nm images during 1730-1930 UT. Alternating bright and dark intensity
641 striations can be seen over North. Slope of these striations indicates towards the south-north
642 movement of GW fronts. (c)-(d) Sample time difference images created from successive
643 images. GW bright fronts 'f1' and 'f2' can clearly be seen separated by a dark trough during
644 1754-1806 UT. (e) Scatter plot of the TEC along the track of IPPs for different GPS satellites
645 over Hyderabad (17.3° N, 78.6° E, mlat. ~12.0° N) during 1700-2000 UT on 16 April 2012.
646 PRN numbers of GPS satellites along with the start time at 1700 UT are marked adjacent to
647 the corresponding IPPs trajectory. G28's trajectory lay close to the south-west sector of the
648 ASAI. (f) TEC variations of a few satellites showing the presence of GWs activity.

649

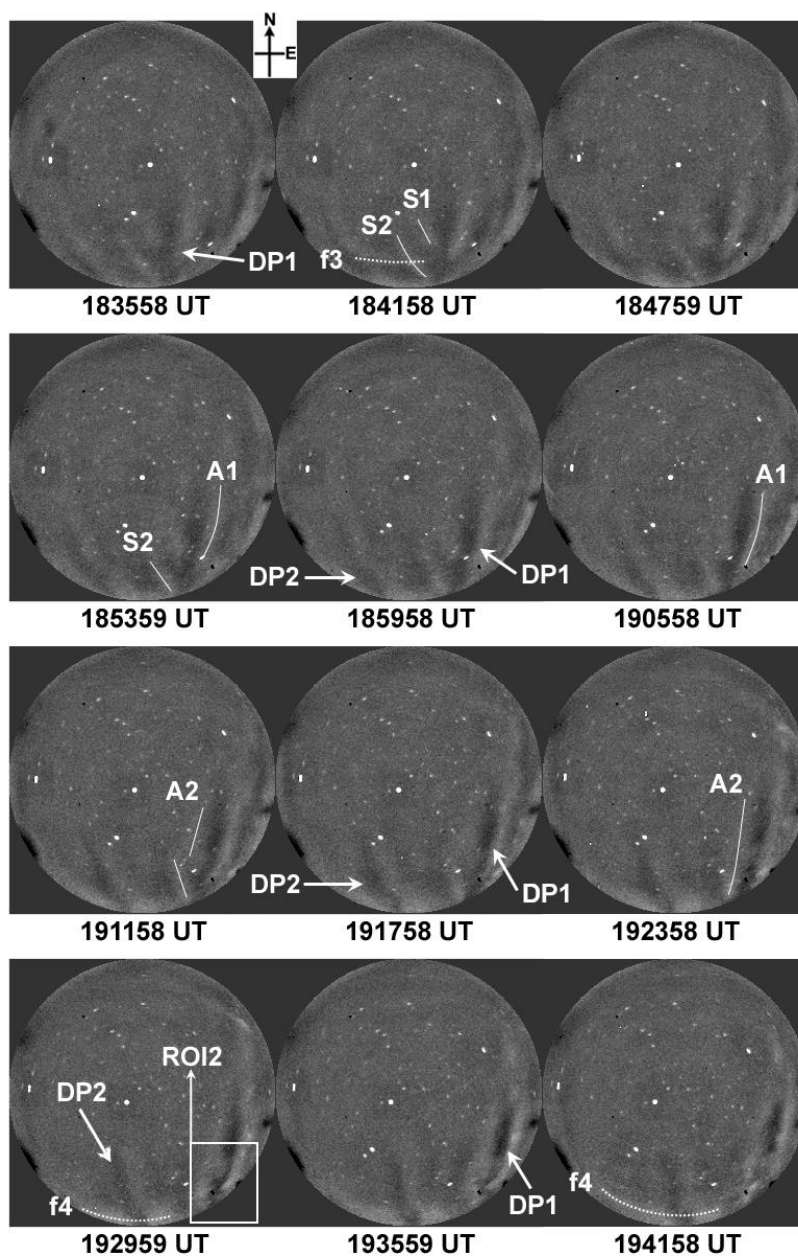


650



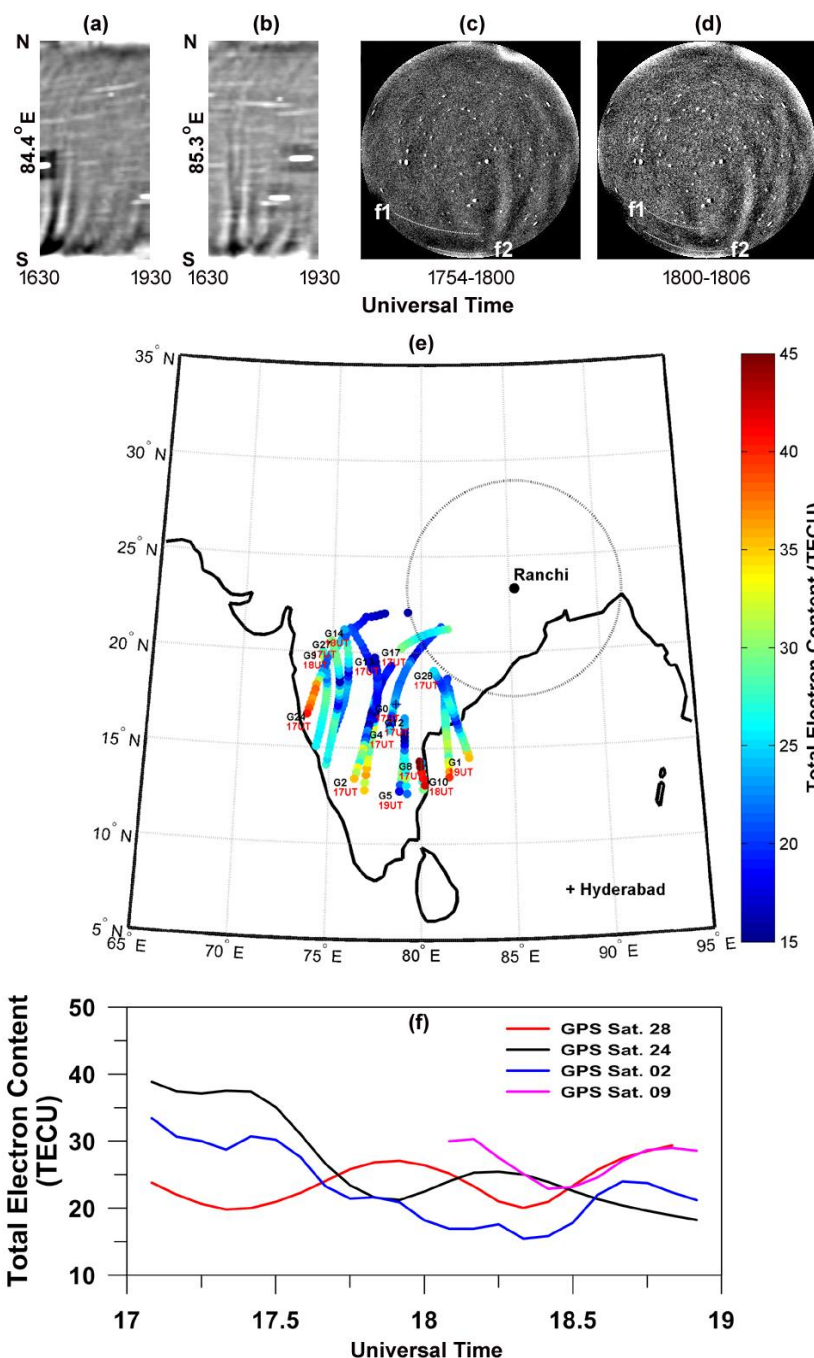
651

652 **Figure 1.** ASAI images during 1742-1830 UT over Ranchi (23.3° N, 85.3° E, mlat. ~19° N)
653 on 16 April 2012. DP1 is the first fossil plasma depletion that showed GWs driven revival.
654 Depletions OD1 and OD2 preceded depletion DP1. ROI1 is the region-of-interest wherein the
655 south-north propagating GW activity and faint signatures of eastward drifting depletion DP1
656 were seen initially. Some noticeable GWs fronts are 'f1', 'f2' and 'f3' (in succession). 'S1'
657 and 'S2' are the fractions of fronts 'f1' and 'f2', respectively, that subsequently got linked to
658 the west wall of depletion DP1.



659

660 **Figure 2.** Same as Figure 1 but for 1836-1942 UT. DP2 is the second fossil depletion that
661 showed GWs driven revival. Some noticeable GWs fronts are ‘f3’ and ‘f4’. A1 and A2 are
662 two arc-shaped regions of airglow enhancement near the east and west wall of depletion DP1.
663 ROI2 is the region-of-interest wherein ambient plasma diffusion occurred across the west
664 wall of depletions DP1.



665

666 **Figure 3.** (a)-(b) North-south (NS) keogram along 84.4° E and 85.3° E longitude generated
 667 from OI 630 nm images during 1730-1930 UT. Alternating bright and dark intensity
 668 striations can be seen over North. Slope of these striations indicates towards the south-north



669 movement of GW fronts. (c)-(d) Sample time difference images created from successive
670 images. GW bright fronts 'f1' and 'f2' can clearly be seen separated by a dark trough during
671 1754-1806 UT. (e) Scatter plot of the TEC along the track of IPPs for different GPS satellites
672 over Hyderabad (17.3° N, 78.6° E, mlat. ~12.0° N) during 1700-2000 UT on 16 April 2012.
673 PRN numbers of GPS satellites along with the start time at 1700 UT are marked adjacent to
674 the corresponding IPPs trajectory. G28's trajectory lay close to the south-west sector of the
675 ASAI. (f) TEC variations of a few satellites showing the presence of GWs activity.